POLITECNICO DI TORINO
Repository ISTITUZIONALE

Permanent Magnet minimization in PM-Assisted Synchronous Reluctance motors for wide speed range

Original
Permanent Magnet minimization in PM-Assisted Synchronous Reluctance motors for wide speed range / Guglielmi, P., Boazzo, B., Armando, E.G., Pellegrino, G.-.M.L., Vagati, A.. - In: IEEE TRANSACTIONS ON INDUSTRY APPLICATIONS. - ISSN 0093-9994. - STAMPA. - 49:1(2013), pp. 31-41. [10.1109/TIA.2012.2229372]

Availability:
This version is available at: 11583/2503190 since:

Publisher:
IEEE

Published
DOI:10.1109/TIA.2012.2229372

Terms of use:

This article is made available under terms and conditions as specified in the corresponding bibliographic description in the repository

Publisher copyright

(Article begins on next page)

01 November 2026

Permanent Magnet minimization in PM-Assisted Synchronous Reluctance motors for wide speed range

P. Guglielmi, B. Boazzo, E. Armando, G. Pellegrino and A. Vagati
Department of Electrical Engineering - Politecnico di Torino
Corso Duca degli Abruzzi, 24 - Torino, 10129 ITALY

***Abstract*— The paper presents a technique to modify the rotor lamination of a PM-assisted Synchronous Reluctance motor, in order to reduce the magnet volume with no side effect on performance. A closed-form analysis, based on a lumped parameter model points out that the magnets quantity can be minimized with a significant saving of material volume and cost. At a second stage, the risk of de-magnetization is evaluated, since the minimized magnets are thinner than the starting ones and work on lower load lines in their respective B-H planes. A feasible drawing is analytically defined, robust against demagnetization at overload, showing that the saving of magnet quantity depends on the maximum current overload and can be significant. The theoretical formulation is validated with finite-element analysis and experiments on a prototype machine.**

I. Introduction

INTERIOR Permanent Magnet (IPM) machines have been extensively studied in recent years because of their good torque density, efficiency and inherent suitability to zero speed sensorless control, due to rotor saliency [1]–[9]. Moreover, it is shown in the literature that enhancing the rotor saliency is beneficial when a large constant power speed range (CPSR) is required [10]. In fact, a large saliency conversely means a relatively low permanent magnet (PM) flux linkage, with the additional advantages of a lower magnet quantity and cost, a lower over-voltage in case of inverter fault and a larger overload capability [11]. The latter characteristic is very welcome in up to date applications, such as electric and hybrid traction [12]. PM-assisted Synchronous Reluctance (PMASR) machines are basically multi-layer IPM machines showing a high saliency and a small per-unit PM flux or, in other words, Synchronous Reluctance (SyR) machines with PMs inserted into the rotor layers.

The design procedure of a PMASR motor generally starts with the design of the multi-layer SyR motor [13], [14]. As a second step, PM pieces are added such to obtain the willed PM flux linkage. When a large CPSR is wanted, the target PM flux linkage is chosen so that the the rated motor current is close to or greater than the characteristic current (1), for the sake of flux weakening capability.

$$I_{rated} \geq I_{char} = \frac{\lambda_m}{L_q} \tag{1}$$

Where I_{char} is the characteristic current, λ_m is the PM flux linkage and the $q-$axis inductance L_q is indicated instead of the $d-$axis one because the considered dq axes are the ones of the SyR machine, also for the PMASR motor.

Once the geometry of the rotor laminations and PM pieces is set, the torque versus speed curve follows, given the current and voltage ratings of the power converter.

In the following it is shown that the same motor performance can be obtained with slightly modified rotor shapes, with reduced amount of PM material. In particular:

- a family of PMASR rotors, all descending from the same starting SyR design, is analytically defined;
- from this family of rotors, the one with the minimum PM quantity is drawn.
- The risk of demagnetization is evaluated leading to a final design, with intermediate PM quantity, compatible with the worst case demagnetizing current condition.
- The reduction of PM quantity is higher for a lower current overload and vice versa.

The basic idea of PM and rotor lamination modification is shown in Fig. 1.

The paper is organized as follows: the PMASR machine design procedure is briefly summarized in Section II to point out how the starting motor is obtained. Then, the PM design modification is described analytically, by a linear, lumped parameters model (Section III). Selected machines are Finite Element (FE) evaluated in Section IV, to validate the analysis and point out local field aspects. Last, experimental results are given for a prototype motor (Section V).

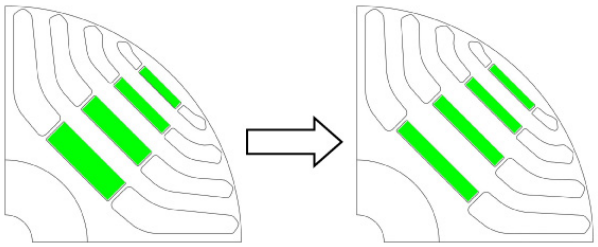


Fig. 1. Example of original and modified rotor geometry. Left: starting design; right: design with reduced PM volume, verified toward de-magnetization at maximum overload.

II. Design procedure of the PMASR machine

As said, the best possible Synchronous Reluctance machine is designed, given the size of the active parts (stack diameter

and length) and the rate of heat removal at the outer stator surface (W/m^2). For standard industrial and traction motors this typically leads to a four pole design, with three or four rotor flux barriers per pole, depending also on the stator slot number [15]. Two key design choices are:

- the rotor diameter x, in per-unit of the stator diameter;
- the air-gap flux density b, in per-unit of the stator yoke flux density.

The product $x \cdot b$ represents the normalized machine flux. When designing the SyR motor, a trade off is generally found between torque and power factor. In fact, a low x would lead to a high torque due to long slots and high electrical loading, but also to a high quadrature inductance that is a lower saliency and rated power factor. Quadrature inductance (L_q) refers to the minimum permeance rotor axis q, as said. Low x figures also increase the copper weight and the end windings length. Similar considerations apply to the b parameter: a large air-gap flux density increases the airgap flux at the expense of a larger recoil iron path needed (stator yoke and teeth, rotor flux guides must be thicker) that, again, lowers the machine saliency and then the power factor.

When the PMs are added to the basic SyR motor, the copper quantity must be also traded-off with the PM cost: the quadrature inductance is apparently less critical in the PMASR than in the SyR motor, since its flux linkage can be compensated with the PM flux and a high power factor is still possible. However, compensating a larger inductance requires more magnets: thus, it is still important to keep L_q as low as possible, as analyzed more in detail in [14], [16].

All considered, the same considerations about x and b made for the SyR motor are also valid for the PMASR, and a reasonable trade-off must be found. The four-poles PMASR machine sketched in Fig. 2 has $x = 0.57$ and $b = 0.58$.

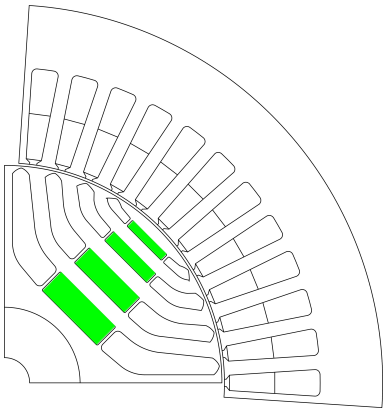


Fig. 2. Starting PMASR machine design: the green-filled areas represent the PM pieces.

As a result, the example machine of Fig. 2 has a good power factor in all its speed range and for a large current range. At continuous current ($25Apk$) the calculated power factor is 0.887 at base speed (3500rpm) and 0.99 at maximum speed (10000rpm). The PM flux linkage is 50% of the rated flux in this case, which is somehow large for a PMASR motor. In fact, this motor is designed for a 100% overload capability, because of the specific application (light traction), so the sizing of the PM flux linkage refers to the overload current (I_{rated} in equation 1 is the maximum inverter current, $50Apk$). At maximum current and base speed, the power factor is still very high (0.898) as it is at maximum speed (0.95). The specifications of the example machine are reported in Table I.

III. Minimization of the PM quantity

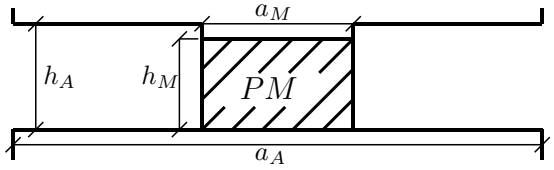
Given the PMASR rotor of Fig. 2, a significant reduction of the PM volume of each layer can be obtained by reducing the thickness of the magnet pieces and filling the space left free by the magnets with iron. The tangential span of the magnets must increase slightly when the thickness decreases, as will be shown, but still the cross-area of the PM gets smaller, to a certain extent. When the shape of one magnet piece is modified, the two structural ribs at its sides move accordingly, as clarified in Fig. 1.

The rotor rearrangement has little practical impact on the machine performance and it is viable for all PMASR motors where only a portion of the flux barriers is occupied by PMs, that is often the case with rare-earth based magnets.

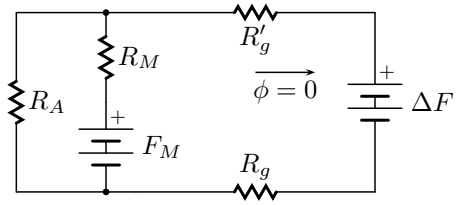
The analytical formulation given in the following refers to a single barrier, and applies to each rotor barrier individually taken, decoupled from all the others. The key-aspect of having the barriers decoupled is related to the specific design approach and *it is not an approximation* of the method.

A. Simplified barrier with no ribs

A simplified flux barrier is first considered, with the structural ribs neglected, to introduce the analysis with a simpler notation. The basic flux-barrier is sketched in Fig. 3(a), in a linearized manner. The equivalent magnetic circuit is in Fig. 3(b).



(a) Linearized geometry of the k-th flux-barrier



(b) Magnetic circuit model

Fig. 3. Simplified barrier model, with the connecting ribs neglected.

The parameters of the equivalent circuit of Fig. 3(b) are defined:

$$R_M = \frac{h_M}{\mu_M \, \mu_0 \, a_M \cdot l} \quad ; \quad R_A = \frac{h_A}{\mu_0 \cdot (a_A - a_M) \cdot l}$$
$$F_M = \frac{B_r}{\mu_0} \cdot h_M \qquad (2)$$

Where R_M is the reluctance of the PM piece, R_A is the reluctance of all the air sections (left and right sides), l is the stack length, μ_0 is the vacuum permeability, $\mu_M \simeq 1$ is the relative permeability of the PM material, set to one for simplicity, and B_r is its remanence. μ_M is set to one for simplifying the notation. The two airgap reluctance terms R_g and R'_g refer to the two airgap portions available for the each flux barrier to recoil flux toward the stator: one path is along the more external flux guide (R'_g) and the other one along the more internal one (R_g). They are not expressed in formulae because not involved in the calculations.

The magneto-motive force (MMF) term ΔF in Fig. 3(b) is representative of the portion of stator MMF related to each layer, according to the staircase approach summarized in Fig. 4 [17]. The peak of the fundamental stator MMF is:

$$\hat{F} = \frac{3}{\pi} \cdot \frac{N}{p} \cdot K_w \cdot \hat{I}_q \tag{3}$$

where the number of turns N and the pole pair number are reported in Table I. The winding factor is 0.925 and $\hat{I}_q$ is the peak of the current component along the *q*-axis (against the magnets). The steps of the staircase are obtained by averaging the fundamental MMF over the rotor teeth at the airgap, and the height of the ΔF steps is reported in Fig. 4 for the example machine.

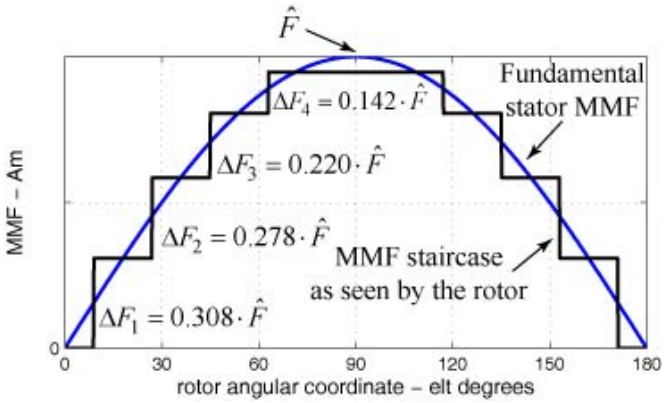


Fig. 4. Definition of the stator MMF portions $\Delta F_1 - \Delta F_4$ relative to the four flux-barriers of the example machine. The stator MMF is aligned against the PM axis.

All the considerations in the following refer to the stator current vector being equal to the *characteristic current* (1), that is also the steady-state three-phase short-circuit condition. It is a known property of all IPM machines that the fundamental flux linkage is null in this condition. It is *a specific property of the design technique we chose that also the flux through each barrier is zero* when the fundamental flux is null [14], as indicated by the $\phi = 0$ annotation in Fig. 3(b). With reference to the basic geometry definitions of Fig. 3(a), the PM cross-area S_M, the thickness ratio y and the span ratio z are introduced (4).

$$S_M = a_M \cdot h_M \quad \text{and} \quad y = \frac{h_M}{h_A} \quad ; \quad z = \frac{a_M}{a_A} \tag{4}$$

The relationship between the two adimensional factors y, z and the PM area is:

$$y \cdot z = \frac{S_M}{h_A \cdot a_A} = \frac{S_M}{K_1} \quad \text{where} \quad K_1 = h_A \cdot a_A \tag{5}$$

The zero-flux condition is analytically expressed as the balance between the two MMF generators in the circuit:

$$F_M = \frac{R_A + R_M}{R_A} \cdot \Delta F \tag{6}$$

After some manipulation of (2) - (6), the PM area at given stator MMF ΔF is expressed as a function of the PM per-unit thickness y:

$$S_M = \frac{K_1\, y^2}{K_2\, y - 1} \quad \text{where} \quad K_2 = \frac{h_A \cdot B_r}{\mu_0 \Delta F} + 1 \tag{7}$$

The relationship (7) is represented in Fig. 5, applied to the four layers of the example motor (Fig. 2). According to the assumptions, equation (7) defines a family of machines, all having the same characteristic current, but slightly different rotor geometry and magnet shape. It is demonstrated in the following that all such machines have also very similar performance in terms of torque an power factor.

The condition $y = 1$ refers to the starting design (Fig. 2), with all the PMs as thick as the flux barriers, that is also the minimum tangential span design (z_{min}), according to (5). The PM area of the starting machine is then:

$$S_{M1} = S_M(y = 1) = \frac{K_1}{K_2 - 1} \tag{8}$$

$$z_{min} = z(y = 1) = \frac{1}{K_2 - 1} \tag{9}$$

As the starting design is the maximum y and minimum z combination, a dual situation is when the PM is so wide to fill all the available tangential space ($z = 1$). The minimum per-unit thickness y_{min} follows:

$$y_{min} = y(z = 1) = \frac{1}{K_2 - 1} \tag{10}$$

Substituting (10) in (7) it is found that the PM area of the thinnest magnet (y_{min}) is equal to the one of the starting magnet (9), as also clear from Fig. 5. Somewhere in between the two extreme designs $y = 1$ and y_{min} the PM area curve has a minimum, found by setting to zero the partial derivative of (7). y_{opt} refers to the minimum magnet area of each layer.

$$\frac{\partial S_M}{\partial y} = 0 \quad \Rightarrow \quad y_{opt} = \frac{2}{K_2} \tag{11}$$

The corresponding PM area $S_{M,opt}$ is:

$$S_{M,opt} = 4 \cdot \frac{K_2 - 1}{K_2^2} \cdot S_{M1} \tag{12}$$

The graphs in Fig. 5 refer to the geometry of the starting design: the dimensions and constants needed for calculations are reported in Table II. It can be noticed from Fig. 5 that the reduction is significant for the PMs of the more internal layers, of bigger size, and quite limited for the most external layer, indicated as *layer 4* in the figure.

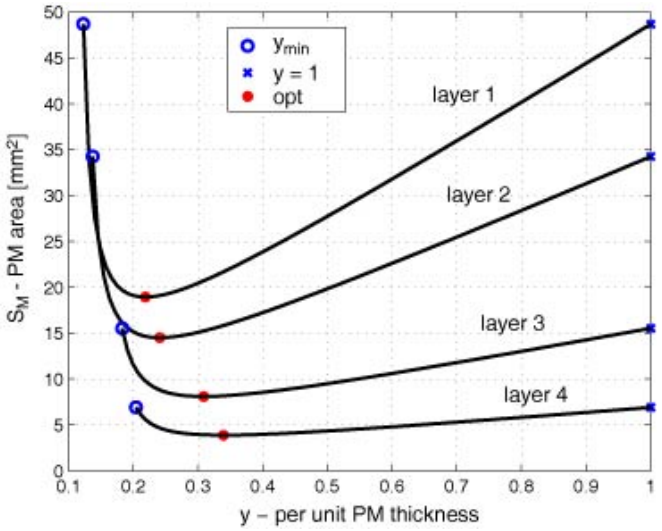
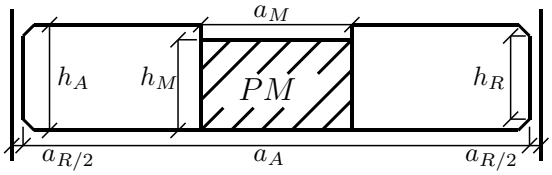


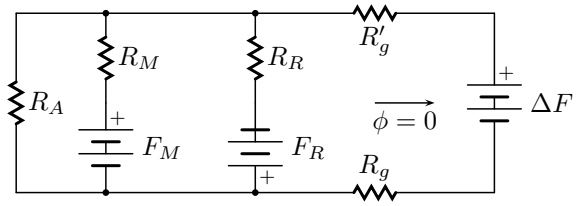
Fig. 5. Permanent magnet area as a function of the PM thickness factor for each of the four barriers of the example motor. Ribs neglected.

B. Flux barrier model considering structural ribs

A more realistic model of the flux barriers must include the mechanical ribs as depicted in Fig. 6(a). The model is formally more complicated but the results are very similar. The two equivalent ribs at the sides of the figure are representative of the combined effect of the outer and inner ribs: their equivalent thickness $a_R/2$ is the sum of the thickness of one radial and one tangential rib. The circuital model is reported in Fig. 6(b).



(a) Linearized geometry of the k-th flux-barrier



(b) Magnetic circuit model

Fig. 6. Flux-barrier model, including the connecting ribs.

All the ribs of one layer are represented in the circuital model by one equivalent MMF (F_R) in series with an equivalent reluctance (R_R):

$$R_R = \frac{h_R}{\mu_R\,\mu_0 \cdot a_R \cdot l} \quad \text{and} \quad F_R = \frac{B_R}{\mu_R\,\mu_0} \cdot h_R \tag{13}$$

The two factors B_R and μ_R refer to the adopted steel grade (M470-65A) and are derived from the saturated part of its magnetic characteristic, as suggested in Fig. 7: the underlying assumption is that all the ribs are saturated at all working conditions (load and no load) of the machine. From experience and FEA verification it turns out that the ribs of this type of machines, when designed as indicated in the previous section, work all around 2 T, either at no-load or load.

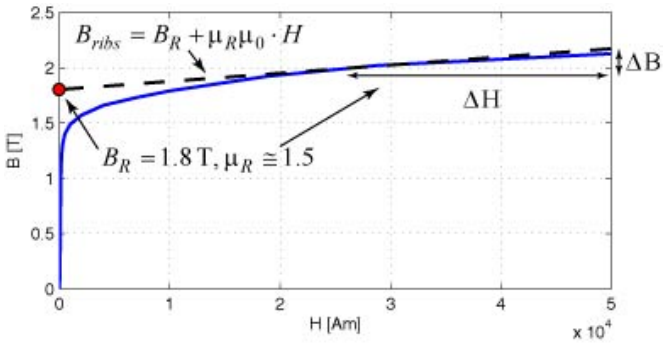


Fig. 7. Identification of the B_R and μ_R parameters for modeling the saturated iron ribs, from the magnetization characteristic of M470-65A silicon steel.

The relationship between the magnet area S_M and the thickness factor y turns out to be:

$$S_{M,r} = \frac{K_1 K_3\, y^2}{K_2\, y - 1} \quad \text{where} \tag{14}$$
$$K_3 = \mu_R \frac{a_R}{a_A} \frac{h_A}{h_R}\left(1 + \frac{F_R}{\Delta F}\right) + 1$$

The subscript r indicates *with ribs*. The K_1 and K_2 factors are the ones already defined in (5), (7), respectively. The new expression (14), with ribs, is very similar to the simplified one (7), apart from the factor K_3. The model without ribs can be obtained from the complete model by setting $K_3 = 1$. The minimum value of y_{min} is now (15), while the optimal thickness (16) is formally identical to the one in (11).

$$y_{min,r} = \frac{1}{K_2 - K_3} \tag{15}$$

$$y_{opt,r} = y_{opt} = \frac{2}{K_2} \tag{16}$$

The PM area of the starting design ($y = 1$) must be also recalculated, and corresponds to the values of the starting machine, that was designed accounting for the ribs effect. The PM areas of the two extreme designs ($y = 1$ and $y_{min,r}$) are no longer equal:

$$S_{M1,r} = \frac{K_1 \cdot K_3}{K_2 - 1} \tag{17}$$

$$S_{Mymin,r} = \frac{K_1}{K_2 - K_3} \tag{18}$$

Finally, the minimum PM area is:

$$S_{M,opt,r} = 4 \cdot \frac{K_2 - 1}{K_2^2} \cdot S_{M1,r} \tag{19}$$

That is formally identical to (12), apart from the $S_{M1,r}$ term that is bigger than $S_{M1,}$ (9) due to the ribs effect: a larger PM area is needed because of the flux leaked through the ribs. The PM cross-area curves are reported in Fig. 9 for the four layers of the example machine, as a function of the PM thickness factor y.

C. Current overload and risk of demagnetization

The risk of demagnetization is now considered. The PMs with minimized area are significantly thinner than the ones of the original machine (that was FEA verified against demagnetization at the time it was designed) and then more prone to demagnetization. Of all the possible machines with reduced magnet volume, it is useful to define which are the feasible ones and which are not, once the maximum current overload is prescribed.

A formulation is proposed, based on the simplified version of the magnetic circuital model of Fig. 6(b) reported in Fig. 8. For the sake of simplicity and conservativeness, the ribs (F_R, R_R) and the air (R_A) branches of the circuit are neglected. Also the airgap reluctances R_g and R'_g are neglected, as they are much less than R_M. The MMF steps produced by the overload current are indicated with ΔF_{OL} and are in general greater than the ΔF steps considered in Fig. 6(b), because the overload current is larger than the characteristic current (1).

The limit of the safe operating region for the magnet grade is the minimum flux-density B_{wc} that the PM grade can withstand without irreversible demagnetization. This is defined according to the PM material datasheet, at the worst case operating temperature.

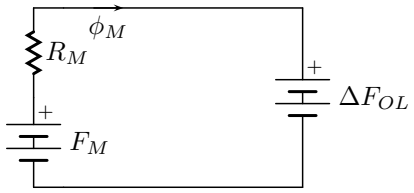


Fig. 8. Simplified barrier model, with the connecting ribs and the air terms neglected.

According to the magnetic circuit in Fig. 8, imposing that the flux density in the PM is B_{wc}, the minimum magnet thickness according to demagnetization is:

$$y_{demag} = \frac{\mu_0 \cdot \Delta F_{OL}}{B_{wc} \cdot h_A} \tag{20}$$

As an example, we set $B_{wc} = 0.5$ T. The MMF steps ΔF_{OL} are calculated for each barrier the same way of ΔF (see Fig. 4 and 3), with augmented current amplitude. In Fig. 9 the formula (20) is applied for two different overload currents: 50 Apk and 100 Apk, showing the demagnetization-safe designs in the two cases. For each flux barrier, the overload current determines a minimum feasible PM thickness, and, as expected, a higher overload requires all the PMs to be thicker.

D. Application of the model to the example machine

The curves of Figs. 5 and 9 refer to the example design of Fig. 2. The main motor data are reported in Table I while Table II is dedicated to the starting PM dimensions and the K_1, K_2, K_3 coefficients, layer by layer, to implement the calculation of the S_M curves.

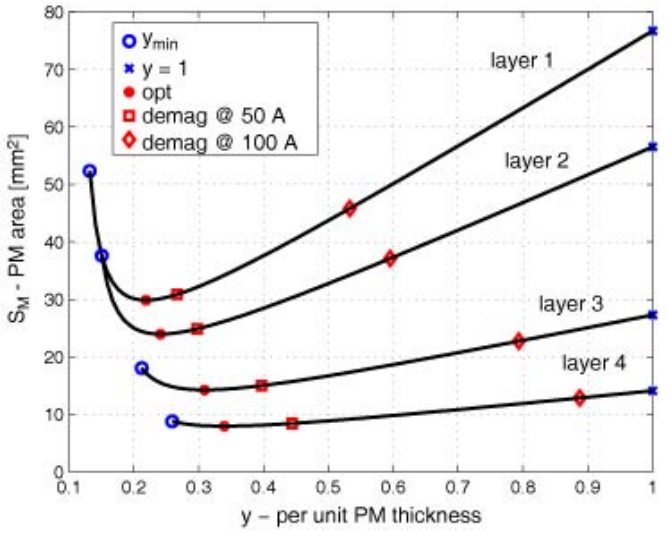


Fig. 9. Permanent magnet area as a function of the PM thickness factor for the four-layer example motor. Ribs accounted.

TABLE I
Main specifications of the example motor.

Cooling type		forced air
Pole pairs		2
Continuous current	Apk	25
Maximum current	Apk	50
Characteristic current	Apk	33
Rated phase voltage	Vpk	230
Back-emf at max speed	Vpk	230
Base speed	rpm	3500
Max speed	rpm	10000
Continuous torque	Nm	18
Max torque	Nm	30
Stator diameter	mm	150
Rotor diameter	mm	86
Stack length	mm	105
Airgap	mm	0.5
Number of turns per phase		80

In Fig. 9 the extreme designs ($y = 1$ and y_{min}) are evidenced together with the optimal design (opt) and the two $demag$ designs corresponding to 50 Apk, 100 Apk and to the predefined PM flux density $B_{wc} = 0.5$ T. As said, the y_{demag} designs have thicker and bigger PMs than the y_{opt} ones. The following conclusions can be drawn:

- the minimum PM quantity is not always feasible, because of demagnetization;
- The larger PMs (layers 1 and 2) lead to a significant saving of magnet weight, also for limited thickness reductions.
- The area of the smaller PMs (layers 3 and 4) changes very little, even for large thickness reductions.
- The larger the overload current is with respect to the characteristic current, the thicker the magnets tend to be, for safety.
- Nevertheless, the reduction of the PM area with respect to the starting design is noteworthy, even for very heavy

TABLE II
Reference design parameters for the starting PM design, as reported in Fig. 2

	$h_M[mm]$	$a_M[mm]$	$K_1[m^2]$	K_2	K_3
layer 1 (inner)	5.1	15.0	$39.7 \cdot 10^{-5}$	9.20	1.58
layer 2	4.1	13.6	$25.0 \cdot 10^{-5}$	8.30	1.65
layer 3	2.4	11.5	$8.5 \cdot 10^{-5}$	6.5	1.76
layer 4 (outer)	1.5	9.2	$3.4 \cdot 10^{-5}$	5.9	2.04

overloads (100 Apk is twice the overload current of the prototype machine);
- Not all the magnets of the starting design ($y = 1$) have the same risk of demagnetization: the outer (and thinner) ones are closer to the 100 Apk - safe designs, while the inner ones have a wider margin. This is consistent with the literature.

E. Effect of slot-leakage and other inductance terms

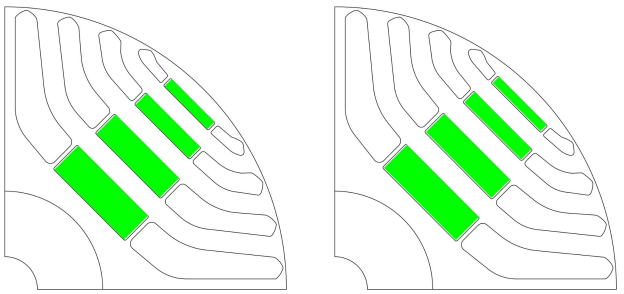
The peak current value considered for all the presented analysis is 46 Apk. From this value the ΔF staircase of Fig. 6(b) have been calculated according to (3) and Fig. 4. It must be underlined that this value is not the actual characteristic current of the motor. In fact, the motor flux linkage includes other inductance terms (slot leakage, zig-zag, etc ..) that increase the L_q term in (1) and are not taken into account in the circuital model for not complicating the equations. In fact, the characteristic current of the family of machines is lower than 46 Apk and it is evaluated to be 34 Apk from FEA results in Fig. 13(b). The correction between the actual I_{char} and the one needed for the magnetic design of the rotor can be pre calculated analytically, as it is the ratio between the L_q with and without the slot leakage and harmonic inductance terms.

IV. FEA COMPARISON OF ROTORS WITH DIFFERENT PM QUANTITIES

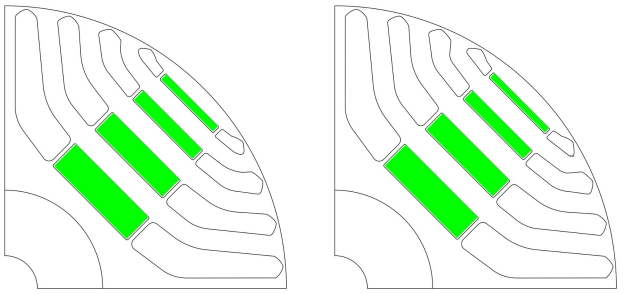
Many rotors have been designed, with reshaped magnets, for evaluating the effect on motor performance and comparing different grades of PM reduction. In Fig. 10 four rotor drawings are presented. The first one (subfigure a) is the starting design, while the other three, that look nearly identical, have all the h_M of the four layers progressively reduced by the same quantity with respect to the starting layer thickness h_A: in subfigure (b) all the PMs are reduced by 0.2 mm, in subfigure (c) by 0.4 mm and in subfigure (d) by 0.6 mm. In turn, they will be indicated as 0.0 (starting design), 0.2, 0.4 and 0.6 in the following.

In Fig. 11 two other rotors are presented, that are the $y_{opt,r}$ (16)and the y_{demag} (20) designs according to the S_M curves in Fig. 9. The *demag* design refers to the 50 Apk overload.

Moreover, the prototype machine, experimentally tested in the following section, is included in the comparison and indicated as *Pt1*. The rotor drawing in this case is between the $0.0 \Leftrightarrow 0.6$ ones, meaning that: not all the layers have been reduced the same but still the rotor geometry is nearly the same of the starting design 0.0.

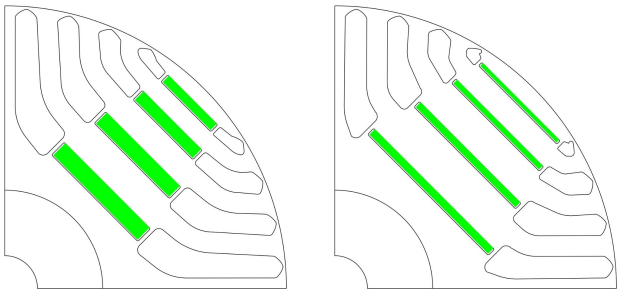


(a) Design 0.0: $h_M = h_A$ mm (b) Design 0.2: $h_M = h_A - 0.2$ mm



(c) Design 0.4: $h_M = h_A - 0.4$ mm (d) Design 0.6: $h_M = h_A - 0.6$ mm

Fig. 10. (a) Starting PM design 0.0. (b)-(d) All PMs made thinner by the same small quantity, respectively 0.2 mm, 0.4 mm and 0.6 mm.



(a) Design (*demag*) (b) Design (*opt*)

Fig. 11. 50 Apk overload safe design (*demag*) and minimum PM design (*opt*).

The terms of comparison are summarized, valid for all the designs:
- PM temperature of 150°C.
- Same stator, air-gap and cooling.
- Structural ribs dimensions: no significant variation in mechanical stress arises from modifying the shape of the PMs and filling the free space with steel, at least with rare-earth magnets that have nearly the same mass density of silicon steel.
- Current amplitude at nominal load: 25 Apk, at base speed ($\omega_b = 3500$ rpm) and maximum speed ($\omega_m = 10000$ rpm) operation.
- Same current phase angles are used at base and maximum speed for all the designs.

A. Performance comparison at no load and rated load

In Table III the following motor outputs are FEA evaluated:
- T_n: nominal torque, at base speed

- PF_n: nominal power factor at nominal torque, base speed
- $T_{\omega_{max}}$: torque at nominal power, maximum speed
- $PF_{\omega_{max}}$: power factor at nominal power, maximum speed
- $E_{\omega_{max+20\%}}$: peak voltage at no load at maximum speed plus 20%
- $S_{M,tot}$: total PM area (all magnets of one rotor pole)

The same quantities are reported in Table IV, this time evaluated with a lumped parameter model, that is usually adopted for the preliminary machine design [14].

TABLE III
Motors performance comparison: FEA

	Pt1	0.0	0.2	0.4	0.6	*Opt*	*Sma*
T_n [Nm]	17.9	17.5	17.7	18.0	18.1	18.8	18.2
PF_n	0.92	0.92	0.92	0.92	0.92	0.92	0.92
$T_{\omega_{max}}$ [Nm]	6.40	6.30	6.40	6.40	6.42	6.50	6.40
$PF_{\omega_{max}}$	0.99	0.99	0.99	0.99	0.99	0.99	0.99
$E_{\omega_{max+20\%}}$ [V]	362	356	363	370	369	509	395
$S_{M,tot}$ [mm^2]	158	174	171	163	153	74	119

TABLE IV
Motors performance comparison: lumped parameters model

	Pt1	0.0	0.2	0.4	0.6	*Opt*	*Sma*
T_n [Nm]	18.7	18.7	18.8	18.8	18.7	19.3	18.8
PF_n	0.89	0.89	0.89	0.89	0.89	0.92	0.90
$T_{\omega_{max}}$ [Nm]	6.70	6.70	6.71	6.72	6.71	6.86	6.74
$PF_{\omega_{max}}$	0.99	0.99	0.99	0.99	0.99	0.99	0.99
$E_{\omega_{max+20\%}}$ [V]	353	350	356	373	362	518	389
$S_{M,tot}$ [mm^2]	158	174	171	163	153	74	119

From Tables III and IV the conclusions are drawn that:

- the *opt* design would save a lot of magnets (-58%) without loss of performance, *except for the no load voltage increase*.
- The feasible machine (*demag*) still obtains a significant magnet saving (-32%), without an appreciable increase of the no load voltage.

According to the design assumptions all the compared motors have the same characteristic current. Then, a higher back-emf (read: a higher no-load flux) indicates also a higher *q*-axis inductance, according to (1): *the machine with less magnets has a lower saliency and consequently a higher uncontrolled generator voltage for the same performance*.

B. Overload condition and demagnetization

For all the seven considered designs the magnets working points are FEA evaluated in two load conditions: nominal current (25 Apk) and overload current (50 Apk). The current vector is oriented against the magnets, as a worst case demagnetizing condition. Tables V and VI report the values of the magnet flux density in the four rotor layers.

Form Table VI it can be seen that the *opt* solution is definitively affected by demagnetization, for standard rare-earth magnet grades at 150°C.

As forecast by the model, the *demag* solution is safe. The flux density is higher than the one assumed in (20) due to the conservative approach of subsection III.C.

TABLE V
FEA evaluated PM flux density @ 25 Apk, in the 4 rotor layers of all the example machines.

	Pt1	0.0	0.2	0.4	0.6	*opt*	*demag*
$B_{pm,1}$ [T]	0.88	0.91	0.89	0.89	0.89	0.58	0.79
$B_{pm,2}$ [T]	0.87	0.91	0.89	0.88	0.87	0.58	0.81
$B_{pm,3}$ [T]	0.82	0.89	0.84	0.80	0.78	0.54	0.81
$B_{pm,4}$ [T]	0.85	0.85	0.77	0.70	0.65	0.47	0.77

TABLE VI
FEA evaluated PM flux density @ 50 Apk, in the 4 rotor layers of all the example machines.

	Pt1	0.0	0.2	0.4	0.6	*opt*	*demag*
$B_{pm,1}$ (inner) [T]	0.82	0.86	0.84	0.83	0.82	0.36	0.69
$B_{pm,2}$ [T]	0.79	0.84	0.81	0.80	0.79	0.34	0.68
$B_{pm,3}$ [T]	0.74	0.77	0.72	0.69	0.67	0.30	0.67
$B_{pm,4}$ (outer) [T]	0.72	0.72	0.63	0.58	0.51	0.26	0.63

C. Cross saturation

The starting design *0.0* and the feasible design *demag* are compared. In fig. 12 the flux density maps at rated torque condition are reported. The same current amplitude (25 Apk) and argument with respect to the d axis and the same mechanical position are considered. Equal color scales are used for the sake of comparison.

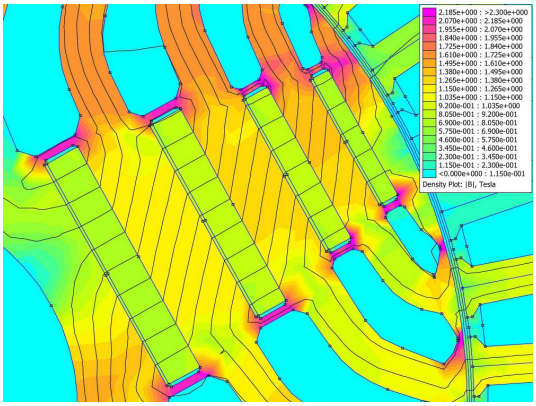
The flux density in the steel around the PMs is quite different in the two cases, in particular for the two more internal layers that are also the more modified. It turns out that the iron flux paths around the PM area are less loaded in the machine with thinner magnets. On the other hand, the flux density in the PMs is slightly lower with thinner magnets.

The FEA calculated flux versus current characteristics are reported for the two machines in Fig. 13. The *demag* design has a larger *d*-flux thanks to the just mentioned effect of the thinner magnets over the rotor steel paths. The starting design *0.0* has a higher no-load flux and *q*-axis inductance (slope of the curves of Fig. 13(b)), as expected from the back-emf comparison at subsection III.A. It is then interesting to notice that the two continuous *q*-flux curves cross each other exactly at zero flux, in Fig. 13(b), that means *they actually have the same characteristic current*. This confirms the proposed analysis and the PM modification criterion, introduced in Section III. The FEA evaluated characteristic current is 34 Apk. To summarize:

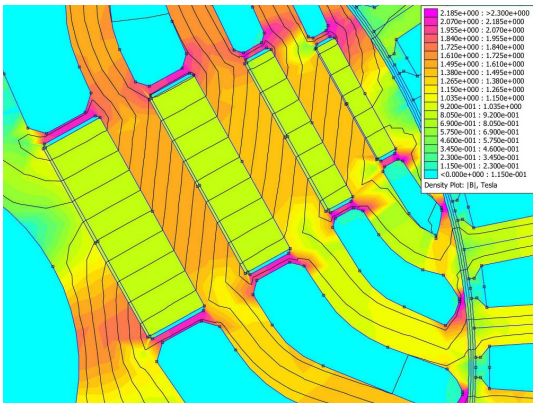
- the thinner magnets release the rotor steel flux paths and then improve the *d*-axis inductance;
- this, at the cost of a reduced robustness against demagnetization, as expected from the model;
- the machine with thinner magnets has the same characteristic current and then nearly the same performance, but obtained via a higher PM-flux linkage and *q*-axis inductance values. This produces a higher no-load back emf in case of inverter fault.

V. Experimental results

Experimental results on the prototype (*Pt1*) shown in Fig. 14 are here presented, to confirm both the lumped parameter



(a) Overload Safe *Sma*



(b) Large Magnet Area *0.0*

Fig. 12. Induction map comparison, FEA results @ nominal load conditions

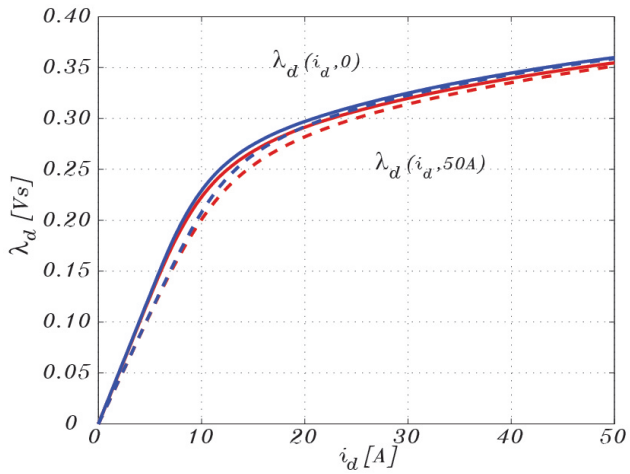
and FEA approaches. The main values for the comparison between FEA, lumped parameters ($L.P.$) and measurements are presented in Table VII. The comparison refers to room temperature of the motor and the magnets (20°C). The three columns show a good agreement. The torque estimation by the lumped parameter model is optimistic because cross-saturation is only partially accounted for. Once this is known, the lumped parameter model shows to be a good instrument for preliminary design.

TABLE VII

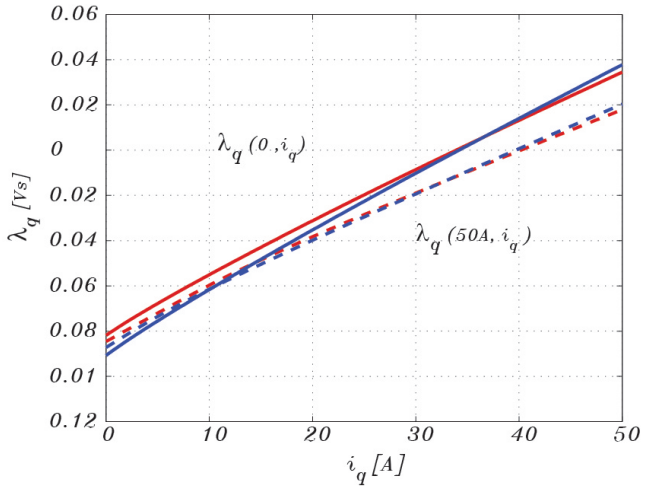
Comparison of FEA, lumped parameters and measuremenst for the prototype motor @ 20°C

	FEA	L.P.	Meas.
$T_{\omega_b,nom}$ [Nm]	18.2	19.7	18.0
$PF_{\omega_b,nom}$	0.96	0.94	0.918
$T_{\omega_m,nom}$ [Nm]	6.50	7.00	6.10
$PF_{\omega_m,nom}$	0.98	0.97	0.98
$E_{\omega_m+20\%}$ [V]	480	473	461

The experimental magnetic characteristics of *Pt1* are shown in Fig. 15, and compared with the FEA and lumped parameter evaluated ones. Fig. 15(b) shows that the lumped parameter model does not take into consideration different rotor effects just evidenced in this paper, such as cross saturation and the related reduction of the d-axis inductance, that is in fact overestimated significantly.



(a) d-axis (min permeance). Dashed lines $i_q = 50A$



(b) q-axis (max permeance). Dashed lines $i_d = 50A$

Fig. 13. FEA calculated flux curves for *demag* (blue) and *0.0* (red) designs, in rotor coordinates dq.

Finite Elements reproduce the measured d fluxes well, while a clear difference exists between the q-axis fluxes. This is due to the 2-dimensional simulations, that do not include the end-windings inductance and lead to FEA curves with a lower differential inductance, despite the correct evaluation of the no-load flux linkage.

VI. Conclusion

An analytical procedure has been defined, for reducing the magnet quantity in PM-Assisted Synchronous Reluctance machines without affecting the torque versus speed performance. The proposed solution introduces a new degree of freedom in the design of this kind of motors. The modified machines show a mitigated local saturation in the rotor flux channels, helping to reduce cross-saturation and the need for a large magnetizing current. A minimum PM volume design exists, but it is not always feasible, due to the risk of demagnetization at overload. Still, a strong PM volume reduction can be obtained, even at heavy overload.

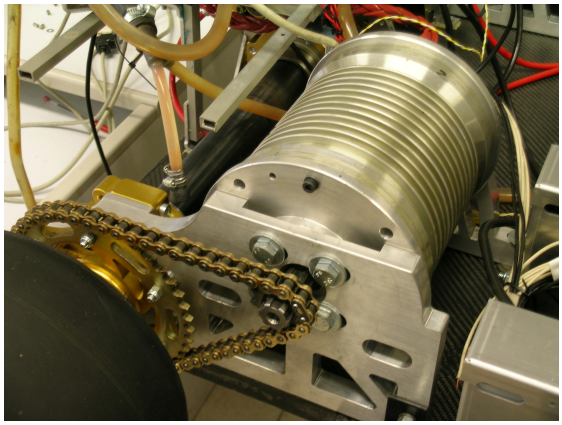
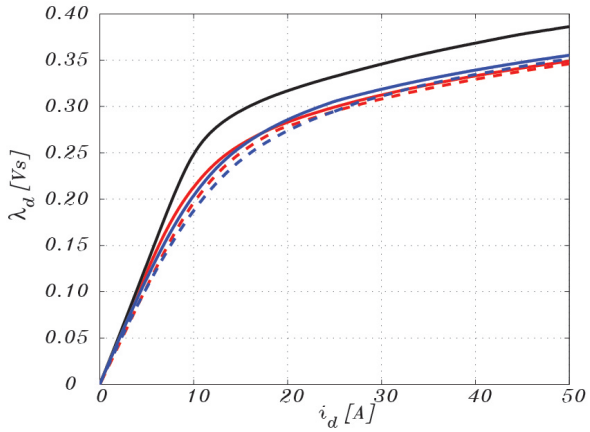
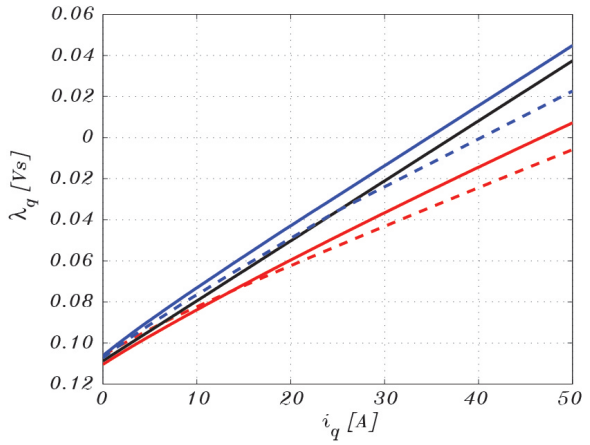


Fig. 14. PMASR prototype built for light traction application

The PMs modifications tend to increase the no load voltage and reduce the saliency of the machine, that is anyway far larger than enough for sensorless control due to the SyR-like rotor. The no-load voltage can be critical in case of fault, in high speed applications. Practical designs have been tested, with FEA, lumped parameters and by experiment.



(a) d-axis (min permeance). Dashed lines $i_q = 50A$



(b) q-axis (min permeance). Dashed lines $i_d = 50A$

Fig. 15. Flux curves of the prototype machine *Pt1*: Measurements (blue), FEA (red), lumped parameters (black)

REFERENCES

[1] E. Lovelace, T. Jahns, and J. Lang, "A saturating lumped-parameter model for an interior pm synchronous machine," *Industry Applications, IEEE Transactions on*, vol. 38, no. 3, pp. 645 –650, 2002.

[2] N. Bianchi, S. Bolognani, D. Bon, and M. Dai Pre, "Rotor flux-barrier design for torque ripple reduction in synchronous reluctance and pm-assisted synchronous reluctance motors," *Industry Applications, IEEE Transactions on*, vol. 45, no. 3, pp. 921 –928, 2009.

[3] C. Jo, J.-Y. Seol, and I.-J. Ha, "Flux-weakening control of ipm motors with significant effect of magnetic saturation and stator resistance," *Industrial Electronics, IEEE Transactions on*, vol. 55, no. 3, pp. 1330 –1340, march 2008.

[4] G. Foo and M. Rahman, "Sensorless direct torque and flux-controlled ipm synchronous motor drive at very low speed without signal injection," *Industrial Electronics, IEEE Transactions on*, vol. 57, no. 1, pp. 395 –403, jan. 2010.

[5] M. Barcaro, N. Bianchi, and F. Magnussen, "Rotor flux-barrier geometry design to reduce stator iron losses in synchronous ipm motors under fw operations," *Industry Applications, IEEE Transactions on*, vol. 46, no. 5, pp. 1950 –1958, sept.-oct. 2010.

[6] S.-H. Han, W. Soong, T. Jahns, M. Guven, and M. Illindala, "Reducing harmonic eddy-current losses in the stator teeth of interior permanent magnet synchronous machines during flux weakening," *Energy Conversion, IEEE Transactions on*, vol. 25, no. 2, pp. 441 –449, june 2010.

[7] A. Consoli, G. Scarcella, and A. Testa, "Industry application of zero-speed sensorless control techniques for pm synchronous motors," *Industry Applications, IEEE Transactions on*, vol. 37, no. 2, pp. 513 –521, mar/apr 2001.

[8] H. Kim, M. Harke, and R. Lorenz, "Sensorless control of interior permanent-magnet machine drives with zero-phase lag position estimation," *Industry Applications, IEEE Transactions on*, vol. 39, no. 6, pp. 1726 – 1733, nov.-dec. 2003.

[9] P. Guglielmi, M. Pastorelli, G. Pellegrino, and A. Vagati, "Position-sensorless control of permanent-magnet-assisted synchronous reluctance motor," *Industry Applications, IEEE Transactions on*, vol. 40, no. 2, pp. 615 – 622, march-april 2004.

[10] M. Barcaro, N. Bianchi, and F. Magnussen, "Design considerations to maximize performance of an ipm motor for a wide flux-weakening region," in *Electrical Machines (ICEM), 2010 XIX International Conference on*, sept. 2010, pp. 1 –7.

[11] G. Pellegrino, A. Vagati, and P. Guglielmi, "Design tradeoffs between constant power speed range, uncontrolled generator operation, and rated current of ipm motor drives," *Industry Applications, IEEE Transactions on*, vol. 47, no. 5, pp. 1995 –2003, sept.-oct. 2011.

[12] G. Pellegrino, A. Vagati, P. Guglielmi, and B. Boazzo, "Performance comparison between surface mounted and interior pm motor drives for electric vehicle application," *Industrial Electronics, IEEE Transactions on*, vol. PP, no. 99, p. 1, 2011.

[13] E. Armando, P. Guglielmi, G. Pellegrino, and A. Vagati, "Optimal design of IPM-PMASR motors for wide constant power speed range," in *Power Conversion & Intelligent Motion Conference*, 22-24 May 2007, nürnberg, Germany.

[14] A. Vagati and P. Guglielmi, *Design, analisys and control of Interior PM synchronous machines*. ISBN 88-7178-898-2, sponsored by IEEE-Electrical Machine Committee, edited by CLEUP, Padova, Italy, 2004, ch. Design of PM-assisted synchronous reluctance (PMASR) motors, pp. 6.1–6.35.

[15] G. Pellegrino, P. Guglielmi, A. Vagati, and F. Villata, "Core losses and torque ripple in ipm machines: Dedicated modeling and design tradeoff," *Industry Applications, IEEE Transactions on*, vol. 46, no. 6, pp. 2381 – 2391, Nov-Dec 2010.

[16] A. Vagati, G. Pellegrino, and P. Guglielmi, "Design tradeoffs between constant power speed range, uncontrolled generator operation and rated current of ipm motor drives," in *Energy Conversion Congress and Exposition (ECCE), 2010 IEEE*, sept. 2010, pp. 4107 –4114.

[17] S.-K. Han, T. Jahns, and W. Soong, "Torque ripple reduction in interior permanent magnet synchronous machines using the principle of mutual harmonics exclusion," in *Industry Applications Conference, 2007. 42nd IAS Annual Meeting. Conference Record of the 2007 IEEE*, sept. 2007, pp. 558 –565.